Evaluation of radar multiple-scattering effects from a GPM perspective, Part II: Model results

Evaluation of Radar Multiple-Scattering Effects from a GPM Perspective. Part II: Model Results

A. BATTAGLIA

Meteorological Institute, University of Bonn, Bonn, Germany

M. O. AJEWOLE

Department of Physics, Federal University of Technology, Akure, Nigeria

C. SIMMER

Meteorological Institute, University of Bonn, Bonn, Germany

(Manuscript received 21 October 2005, in final form 17 March 2006)

ABSTRACT

Multiple-scattering effects as sensed by radars in configurations useful in the context of the Global Precipitation Mission (GPM) are evaluated for a range of meteorological profiles extracted from four different cloud-resolving model simulations. The multiple-scattering effects are characterized in terms of both the reflectivity enhancement and the linear depolarization ratio. When considering the copolarized reflectivity in spaceborne configurations, the multiple-scattering enhancement becomes a real issue for K_a-band radars, though it is generally negligible at the K_u band, except in meteorologically important situations such as when high rain rates and a considerable amount of ice are present aloft. At K_a band it can reach tens of decibels when systems of heavy cold rain are considered, that is, profiles that include rain layers with high-density ice particles aloft. On the other hand, particularly at 35 GHz, high values of the linear depolarization ratio are predicted even in airborne configurations because of multiple-scattering effects. This result should allow the observation of these features in field campaigns.

1. Introduction

In Battaglia et al. (2006, hereinafter Part I) a numerical model to compute multiple-scattering (MS) contributions in precipitation radar signals based on the vector radiative transfer equation was presented. The model accounts for general radar configurations such as airborne/spaceborne/ground based and monostatic/bistatic and includes the polarization and the antenna pattern as particularly relevant features. The model has been validated by comparing the results obtained with analytical solutions. It has been applied to evaluate general features of MS effects by studying the penetration of the radar signal into a uniform hydrometeor layer.

Corresponding author address: Alessandro Battaglia, Meteorological Institute, University of Bonn, Auf dem Hugel, 20, 53121 Bonn, Germany.
E-mail: batta@uni-bonn.de

To predict MS effects for tangible applications, it is necessary to consider realistic vertically inhomogeneous profiles. Kobayashi et al. (2004) investigated MS effects at 94 GHz for a uniform rain layer considered to coincide with one radar range bin (i.e., they have assumed the thickness of the layer to be equal to the radar vertical resolution). Marzano et al. (2003) analyzed MS effects for generic radar bins consisting of intense and heavy rain profiles. In these conditions, Marzano et al. (2003) showed that a huge MS effect is present at 35 GHz (see their Fig. 4, right panels) that can practically compensate for the strong attenuation resulting from intense and heavy rain types. This has very strong implications for the retrieval algorithms. However, as demonstrated in Battaglia et al. (2005a), Part I, and Kobayashi et al. (2004), the antenna pattern can play an important role in reducing the magnitude of the MS effects. Battaglia et al. (2005a) evaluated this factor for the same intense and heavy convective rain types of Marzano et al. (2003) and concluded that MS

effects vanish when passing from typical spaceborne horizontal resolutions on the order of 4–5 km to very high resolution on the order of hundreds of meters. These considerations raise the question of whether airborne field campaigns preparatory to the launching of the Global Precipitation Mission (GPM; e.g., Durden et al. 2003; Heymsfield et al. 2000; Geerts and Dawei 2000) can be conclusive in assessing the importance of MS effects. The GPM is a follow-on and an expanded mission of the Tropical Rainfall Measuring Mission (TRMM), and it is one of the next Earth observation satellite programs that will measure global precipitation with improved temporal resolution and spatial coverage (information was available online at http://gpm.gsfc.nasa.gov/).

Because noticeable MS effects are expected in optically thick regions (like those shown in section 5 of Part I), they are typically present in regions of strong attenuation and, as such, in regions often characterized by signals below the minimum detection threshold (MDT). Attenuation is particularly important for ground-based radars at frequencies in and above the X band and for spaceborne radars at frequencies in and above K_a band. In heavy rain, reflectivity information can become completely lost from large portions of a radar scan. For example, at K_a band the attenuation (dB km^{-1}) is approximately linearly dependent on the rain rate (mm h^{-1}), with a proportionality factor equal to 0.2 (see Lhermitte 1990); thus, a 2-km-thick, 20 mm h^{-1} layer produces a two-way attenuation of 16 dB. Only the MS signal has to be considered when the total return is actually detectable.

It is the main purpose of this paper to extend the analyses performed in Battaglia et al. (2005a) to a range of different realistic meteorological situations and different radar configurations that are applicable to or useful in the context of the GPM and to evaluate the cases in which MS effects are detectable. For this purpose, the Monte Carlo code described in Part I has been exploited to perform simulations for many different realistic profiles extracted from some cloud-resolving models (CRM) briefly described in section 2. The study investigates, in particular, when MS can play a relevant role in spaceborne radars using typical GPM configuration and in airborne configurations to be adopted in GPM preliminary campaigns as well (see section 3). The results obtained from these simulations have finally driven the idea of a proposal for better understanding of the MS within the context of airborne campaigns. This is illustrated in section 4. Conclusions and recommendations for future work are drawn in section 5.

2. Cloud-resolving models

To simulate radar backscattering profiles, simulations from the Goddard Cumulus Ensemble (GCE) model (see Tao and Simpson 1993 and Tao et al. 2003 for details) of a tropical squall line, a mid-Atlantic warm and cold front, and a convective system over the Amazon catchment area at different instants of time have been exploited. Cloud-resolving models represent a unique tool for use to understand the dynamical and radiative processes inside clouds. In particular, they provide realistic hydrometeor profiles and temperature and humidity vertical structures for mesoscale systems with very high horizontal (down to 2 km) and vertical (500 m in the lower troposphere) resolutions. In the GCE CRM, six hydrometeors are considered, including uniform-size cloud droplets (radius 10 μm) and ice crystals (radius 10 μm), raindrops, graupel (density 0.4 g cm^{-3}), and snow (density 0.1 g cm^{-3}), with the latter three hydrometeor classes having exponential size distribution with a fixed intercept parameter N_0. For rain, this intercept is always equal to 1.6×10^4 m^{-3} mm^{-1} (Marshall and Palmer 1948); for graupel and snow, this parameter depends on the CRM. In our computations we have always assumed the intercept values of the Large-Scale Biosphere–Atmosphere Experiment in Amazonia (LBA) simulation—that is, N_0 equal to 1.6×10^4 and 3.2×10^4 m^{-3} mm^{-1} for graupel and snow, respectively. Mixed-phase hydrometeors are not included.

Selected mesoscale systems

The first scenario (Fig. 1) for the simulations is a "deep convective" case simulating a severe squall line (SL) over the tropical ocean. The trailing edge of the cloud system is aligned along the north–south direction, and the anvil extends westward. As the squall line evolves, the coldest cloud tops in some cells dislocate from the leading edge to the top anvil, thereby producing tilted systems (see Hong et al. 2000). The GCE-simulated squall line reaches 18 km in height, with the rain layers extending up to 6 km and precipitation intensities reaching about 100 mm h^{-1}.

The second scenario (no figure) represents a deep convective system (with freezing level between 4 and 5 km) developing during the LBA. The system is characterized by few convective cells with precipitation intensities reaching up to 70 mm h^{-1}. One important feature is the large amount of graupel inside the convective cells (having integrated columnar graupel contents of as much as 30 kg m^{-2}).

The third scenario (Fig. 2) is a mid-Atlantic cold front (CF), which is characterized by shallow convec-

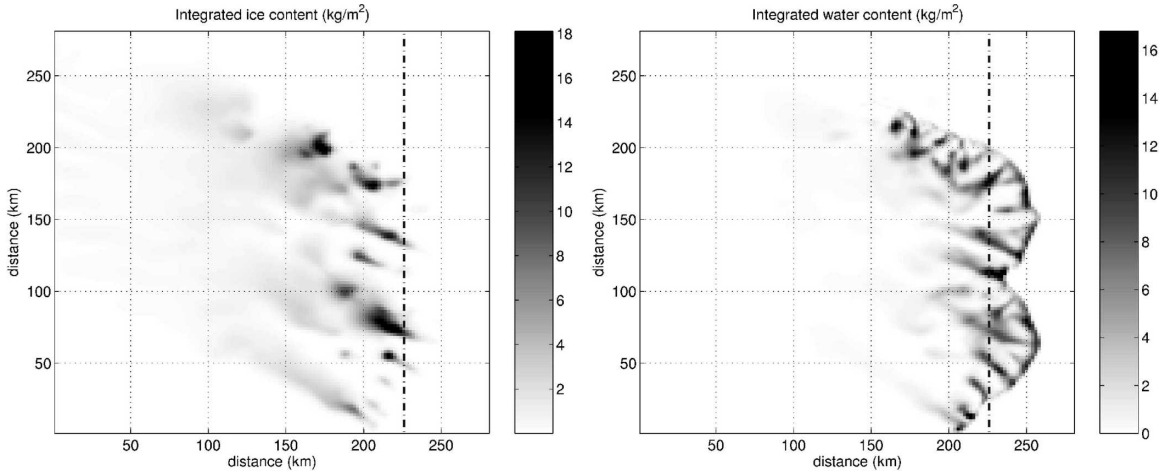

FIG. 1. Total integrated (left) ice and (right) water for the squall-line simulation at $t = 480$ min (case 1).

tion and large stratified areas with moderate to low precipitation. The presence of rainbands and other features make this cloud system similar to frontal systems in extratropical cyclones that greatly affect the European and Mediterranean meteorological patterns. The cold-front simulation is characterized by prefrontal shallow convection and well-developed rainbands aligned with the frontal line along the southwest–northeast direction. Precipitation intensity reaches 50 mm h^{-1} in the cells ahead of the front, and the rainfall intensity produced by postfrontal rainbands does not exceed 30 mm h^{-1}. The stratiform region extends over thousands of square kilometers toward the east; it is particularly rich in snow aloft and shows precipitation rates of less than 10 mm h^{-1} at the ground.

The mid-Atlantic warm front (WF), our fourth case (no figure), represents situations of moderate and widespread rain, a situation that is frequent in midlatitude regions. The system is weakly forced by subsynoptic motion and is totally free from small-scale convective developments. In this case, the rain rate is mostly lower than 10 mm h^{-1}, with a peak of about 50 mm h^{-1} that is a few square kilometers wide. The horizontal structure of the cloud shield shows less spatial variability and a lower vertical extent in comparison with the cold front. The ice content of the warm front is lower than that in the cold front by a factor of 2 (especially in the graupel content), which will affect the radar signal. It is clear that both frontal systems (cases 3 and 4) develop vertically much less than do the squall line and the deep convection (cases 1 and 2)—for example, their freezing level is always lower than 3.5 km.

The four CRM simulations span a wide set of cloud structures and precipitation types; therefore, our data-

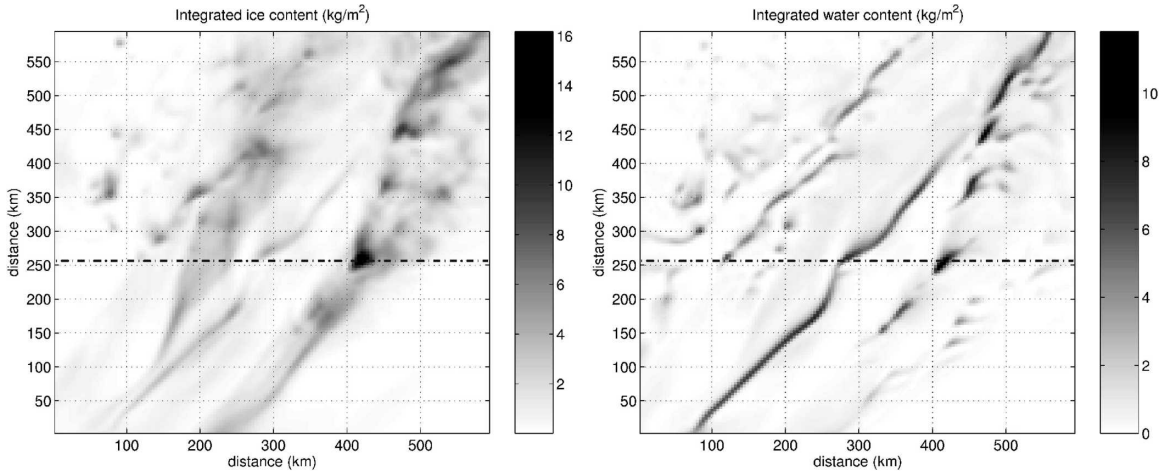

FIG. 2. Total integrated (left) ice and (right) water for the cold-front simulation at $t = 604$ min (case 3).

TABLE 1. Characteristics of spaceborne radars for concluded and future missions according to Kummerow et al. (1998), Iguchi et al. (2002), and Ingmann (2004).

Mission name	Radar frequency (GHz)	Satellite altitude (km)	Radar beamwidth	Horizontal resolution (km)	Best MDT (dBZ)
TRMM	13.8	350	$0.71° \times 0.71°$	4.3	17
GPM	13.8	400	$0.7° \times 0.7°$	4.9	17
GPM	35.5	400	$0.7° \times 0.7°$	4.9	12
EGPM	35.9	500–675	$0.5° \times 0.5°$	4.3	−5 to 5

base should be appropriate to analyze the importance of MS effects in both midlatitude regions and tropical regions.

3. Multiple-scattering results

Single-scattering and MS apparent reflectivities [defined by Eq. (8) in Part I] have been computed by simulating the overpass of a satellite/airplane, equipped with a nadir-looking radar, in north–south and east–west directions for the four mesoscale systems. As reference values for the radar altitude, antenna beamwidth, and MDT, the characteristics of the TRMM precipitation radar (PR) and the dual-wavelength and 35-GHz precipitation radars envisaged for GPM and European GPM (EGPM) have been adopted. The relevant characteristics of these spaceborne instruments are summarized in Table l. Typical airborne radars used in GPM field campaigns have similar frequencies and typical antenna beam widths of 3.8° and 4.8° at 13 and 35 GHz, respectively. If not specified differently, all simulations are performed with radiation transmitted and received in the same linearly polarized state; that is, the reflectivities are copolarized signals.

a. Vertical cross-sectional analyses

The top-left panel of Fig. 3 shows the hydrometeor vertical cross section corresponding to an overpass in the south–north direction at $x = 226$ km over the SL of case 1 (corresponding to the dashed line shown in Fig. 1). The dashed–dotted line in Fig. 3 indicates the freezing-level height and roughly separates the solid-phase from the liquid-phase hydrometeors. Because no brightband model is included, there is a region in which both phases are present. The cross section includes six main rain shafts located around 50, 70, 110, 140, 170, and 200 km. Analogous hydrometeor cross sections for the LBA, the CF, and the WF are depicted in the other three panels of Fig. 3. The freezing-level height is clearly much higher for SL and LBA than for CF and WF; the columnar water contents are consequently substantially larger.

The upper panels of Fig. 4 shown the extinction coefficient and the single-scattering (SS) albedo evaluated at 13.8 GHz corresponding to the SL profile depicted in the top-left panel of Fig. 3. The upper panels of Fig. 5 similarly show the simulated SS properties (top left: extinction coefficient; top right: SS albedo; center left: g parameter) at 35.5 GHz. At 13.8 GHz the mean free path is always higher than 2 km, and the SS albedo remains lower than 0.2 almost everywhere while the g parameter (not shown) stays around zero (between −0.1 and 0.08). At 35.5 GHz the extinction coefficient is bigger by roughly a factor of 4. The SS albedo exceeds 0.4 in most parts of the cross section while the g parameter rises to values as high as 0.35 inside the ice convective cores. As discussed in section 5 of Part I, all of these increases favor MS effects. Therefore, at K_a band MS effects are more likely to be observed.

The plots of the MS apparent copolarized reflectivities Z_a^{MS} are shown in the bottom-left panel in Fig. 4 and center-right panel in Fig. 5, and the MS enhancement (with respect to the SS reflectivities Z_a^{SS})

$$\Delta Z_a^{MS} \equiv Z_a^{MS} - Z_a^{SS} \tag{1}$$

is shown in the bottom-right panel of Fig. 4 and in the bottom panels of Fig. 5. Note that, whereas at 13 GHz the MS enhancement is drawn for a PR configuration (0.7° beamwidth, 350-km altitude; see bottom-right panel of Fig. 4) only, at 35 GHz it is evaluated for both a spaceborne (0.5° beamwidth, 600-km altitude; see bottom-left panel in Fig. 5) and an airborne configuration (4.8° beamwidth, 20-km altitude; see bottom-right panel in Fig. 5).

In the MS copolarized reflectivity and MS enhancement panels of Figs. 4–5, the dashed lines represent the MDT contour levels for Z_a^{SS}, which have been fixed to 10 and 0 dBZ at 13 and 35 GHz, respectively. The Z_a^{MS} MDT contour levels are not shown because they can be deduced from the plot and its color bar; they obviously coincide with the Z_a^{SS} contour levels where MS enhancement is negligible (i.e., always at the top boundary of the detected area). The presence of MS generally

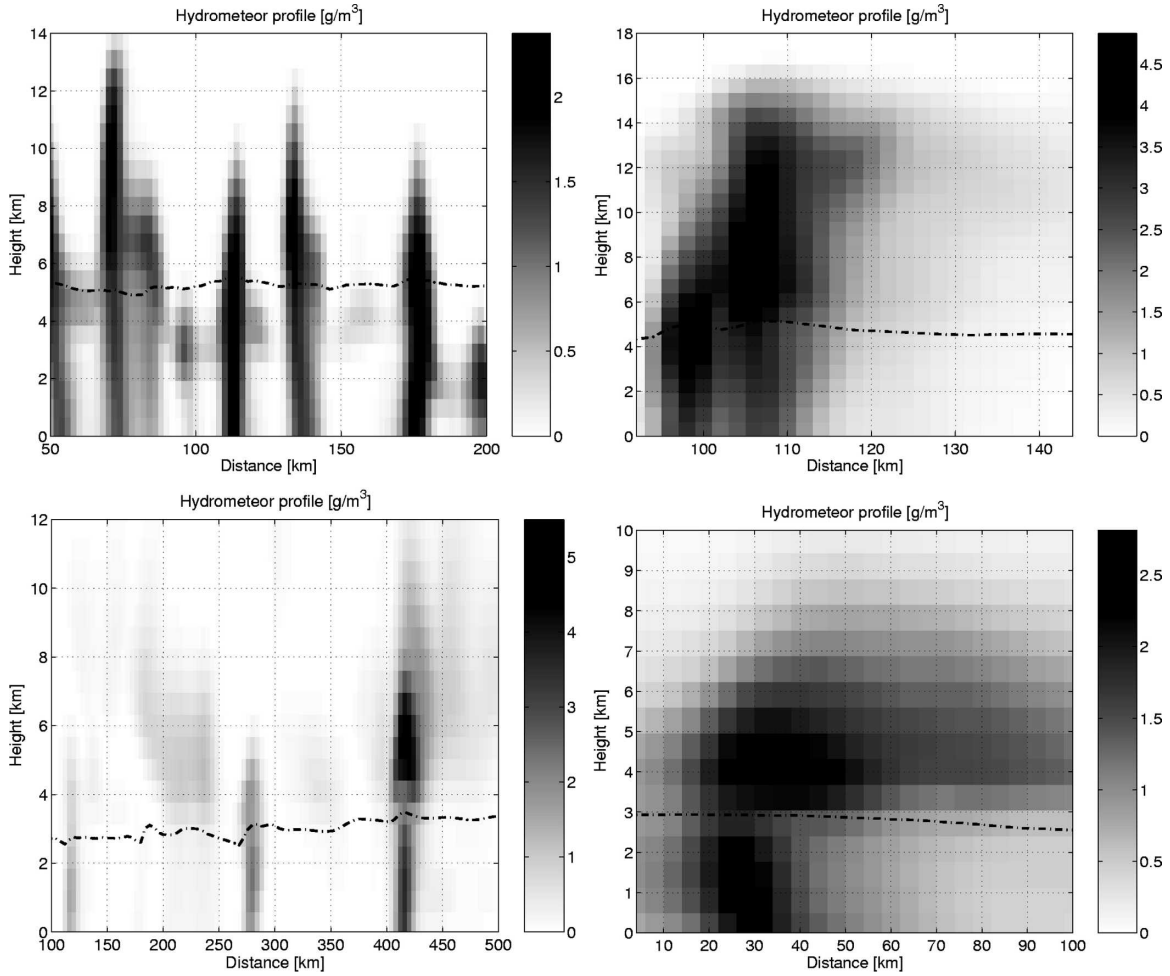

FIG. 3. Cross section of the total hydrometeor density profile for the four different mesoscale systems [(top-left) SL, (top-right) LBA, (bottom-left) CF, and (bottom-right) WF] considered in this study. The dashed–dotted line represents the freezing-level altitude.

increases the total area of detectable regions because, by definition, $Z_a^{\mathrm{MS}} \geq Z_a^{\mathrm{SS}}$, but in an appreciable way only when the Z_a^{MS} and Z_a^{SS} MDT contour levels are different. To have better dynamics at small values, the ΔZ_a^{MS} color-bar scale is set to a maximum value of 30 dB (higher values are reached only at 35 GHz); moreover, it is plotted only in regions with Z_a^{MS} values higher than the MDT. Therefore, white regions in the panel represent ΔZ_a^{MS} that corresponds either to undetectable area or to a region in which the MS enhancement is negligible.

At 13 GHz in the PR configuration (0.7° beamwidth and 400-km altitude) practically no MS is seen; in fact, in the bottom-left panel of Fig. 4 the 10-dBZ contours for the SS follow the same contour level as those of the MS signal. In the bottom-right panel of Fig. 4 the ΔZ_a^{MS} signal for this typical spaceborne configuration has at most 0.9 dB. No airborne configuration is shown in Fig. 4 because the effect is even lower in this case. On the other hand, at 35 GHz the MS effect becomes important both in a spaceborne configuration (with 0.5° beamwidth at 600 km, i.e., 5-km footprint diameter) and in an airborne configuration with 4.8° beamwidth at 20-km altitude (bottom-left and bottom-right panels, respectively, in Fig. 5). This airborne configuration corresponds to a spatial resolution of 1.25 km at 5-km altitude. It is obvious that the MS effect is stronger in the spaceborne configuration because of the larger footprint. Some regions that are theoretically under the MDT when only SS is considered become detectable when all scattering-order contributions are taken into account (see right-middle panel of Fig. 5). This can be seen by looking at the different rain shafts in the region close to the ground where ΔZ_a^{MS} signal is plotted in regions that provide an SS signal below the MDT. For instance, in the spaceborne (airborne) configuration the rain shaft around 70 km (see bottom panels of Fig. 5) provides a MS signal above MDT down to the

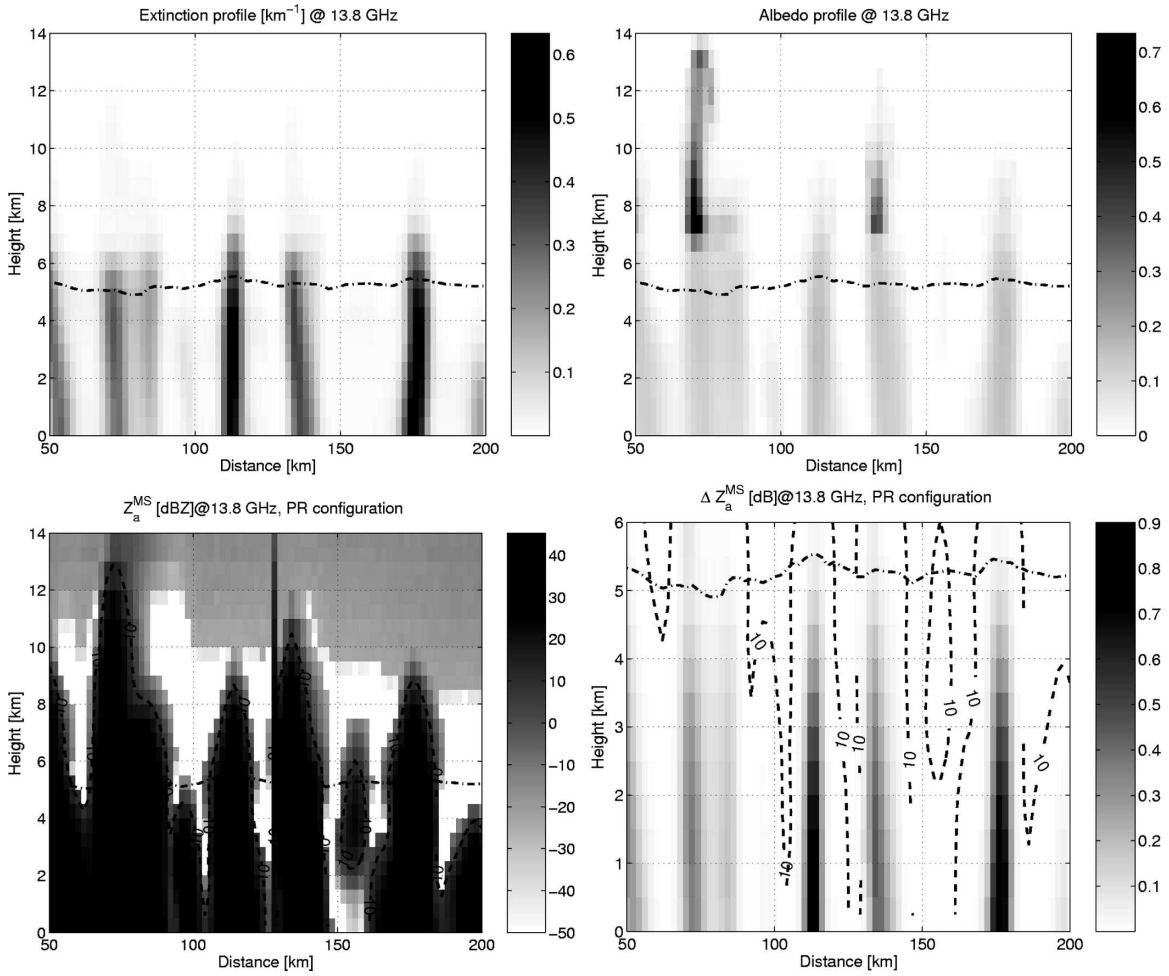

FIG. 4. (top-left) Extinction coefficient (km^{-1}) and (top-right) SS albedo evaluated at 13.8 GHz for the SL cross section in south–north direction at $x = 226$ km. The corresponding hydrometeor density profile is shown in the top-left panel of Fig. 3. The dashed–dotted line represents the freezing-level altitude. (bottom-left) The MS reflectivity and (bottom-right) MS reflectivity enhancement evaluated for a PR configuration (0.7° beamwidth and altitude of 400 km). Dashed lines represent the MDT contour level for the SS reflectivity.

ground (1.5 km). On the contrary, the SS signal is above the MDT only down to 3 km.

An analysis similar to that performed for the SL system in Figs. 4–5 is conducted for an LBA cross section through a heavy-convective-rain cell (shown in the top-right panel of Fig. 3) in Figs. 6–7. The general behavior of the scattering properties is essentially the same as before. However, because of the higher ice-phase hydrometeor content, as shown in the SS albedo panels, a widespread scattering region is present above the freezing level (dashed–dotted line). The extinction coefficient now reaches up to 1.1 and 5 km^{-1} at the two frequencies investigated. As a consequence, MS effects are more consistent in the LBA than in the SL system (case 1). The MS effect at 13 GHz reaches up to 4.5 dB. This corresponds to a deep graupel cell (see top-right panel of Fig. 3) characterized by very high hydrometeor content (up to 4.5 g m^{-3}). These hydrometeor profiles have therefore to be considered as very extreme cases in which the MS is strongly enhanced. Even at 13.8 GHz, values of 3–4 dB for the MS effect appear in TRMM-like configuration.

As revealed by the bottom panels in Fig. 7 the MS is much bigger at 35 GHz: the large part of the region below the freezing level is very often undetectable in the SS approximation (see the dashed line corresponding to the 0-dBZ contour for the SS signal in the bottom-left panel of Fig. 7) while it provides an apparent MS signal that is always above the MDT for spaceborne systems (except at the bottom-left corner at the blank pixel). In airborne configuration this is only partly true (cf. the bottom panels in Fig. 7): almost one-third of the

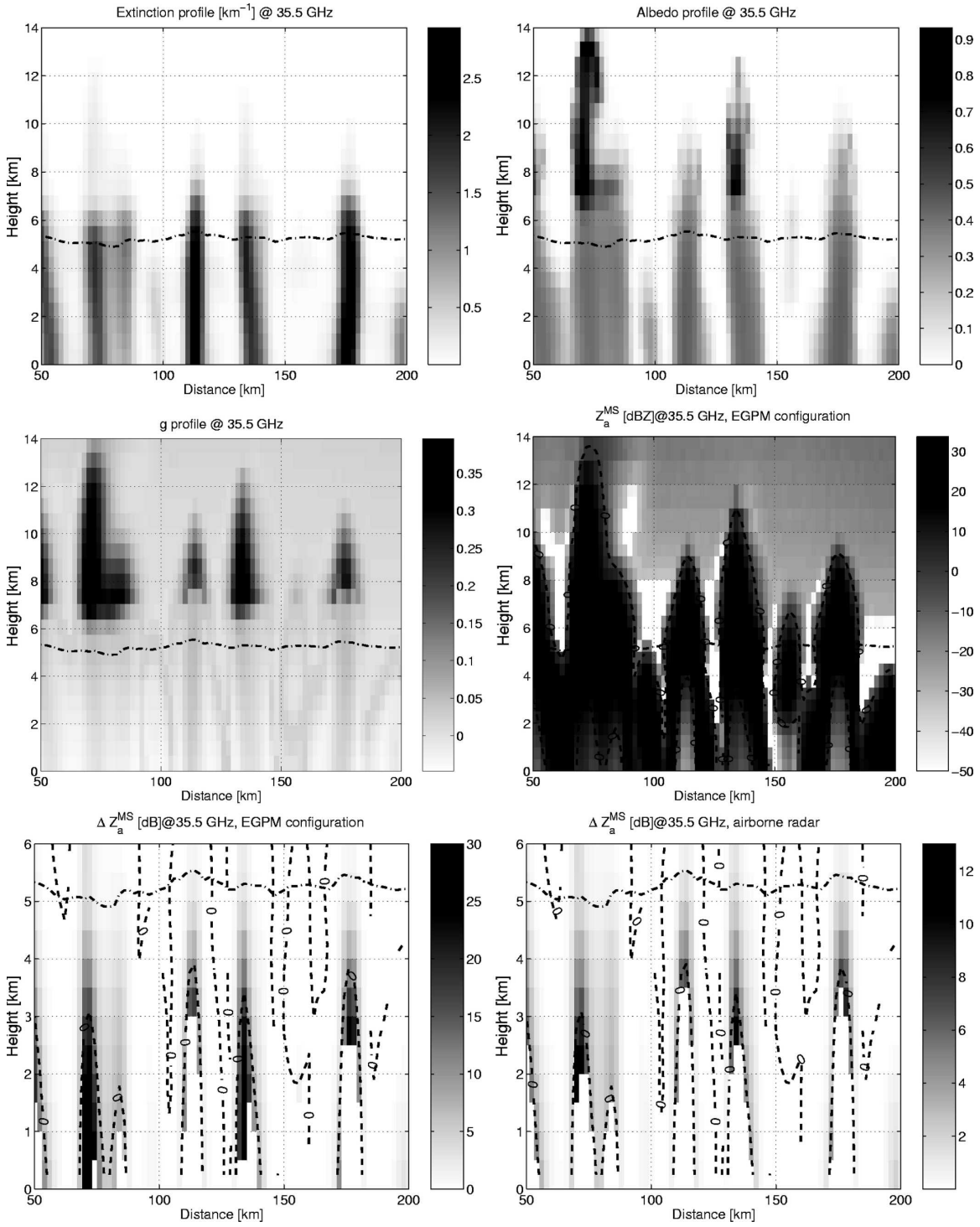

FIG. 5. SS properties and radar quantities evaluated at 35.5 GHz for the same SL cross section as that in Fig. 4. (top-left) Extinction coefficient (km^{-1}) and (top-right) SS albedo. (middle-left) Asymmetry parameter and (middle-right) MS reflectivity evaluated for an EGPM configuration (0.5° beamwidth and altitude of 600 km). MS reflectivity enhancement evaluated (bottom-left) for an EGPM configuration and (bottom-right) for an airborne system (4.8° beamwidth and altitude of 20 km). Dashed lines represent the MDT contour level for the SS reflectivity.

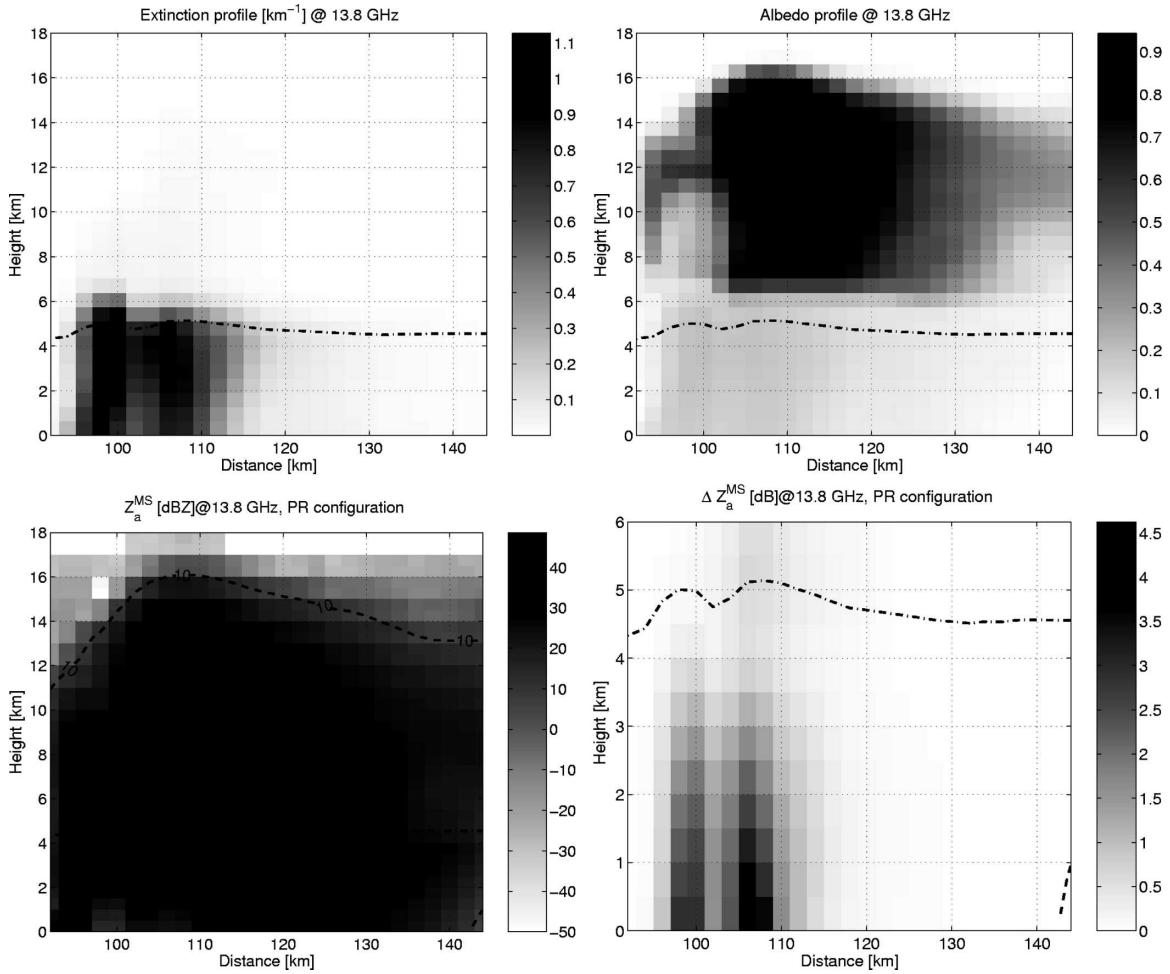

FIG. 6. Same as Fig. 4, but for the LBA cross section in the south–north direction at $x = 134$ km. The corresponding hydrometeor density profile is shown in the top-right panel of Fig. 3.

rainy region does not provide any apparent detectable signal (and therefore is blank).

Similar analyses are conducted for a CF and a WF cross section with hydrometeor profiles depicted in the bottom panels of Fig. 3. For 13 GHz (not shown), the MS effect reaches up to 1.3 dB in correspondence to the area around $x = 410$ km for the CF and up to 0.45 dB in correspondence to the area around $x = 30$ km. Figures 8–9 show the results at 35.5 GHz for these two vertical cross sections. Though the freezing level and the total depth of the hydrometeors are now considerably lower than in the SL and the LBA cases, MS effects can be remarkable in these systems and in correspondence to regions rich in ice-phase hydrometeors (like the denser graupel). For instance, the cold-front prefrontal cell around $x = 410$ km (see also Fig. 2) that produces almost 75 mm h^{-1} rain at the ground produces an MS enhancement close to the surface that is higher than 30 dB in both the spaceborne and the airborne configurations, as shown in the bottom panels of Fig. 8. As a result, while the SS signal close to the surface is strongly damped by attenuation and is well below the MDT (see the middle-right panel in Fig. 8) the MS remains well above the MDT. Although the MS effect is lower, similar effects are visible in the warm front. The rainy cell around $x = 30$ km plotted in the top-left panel of Fig. 9 hits up to 50 mm h^{-1} and produces an MS enhancement as high as 22 and 12 dB in the pixel immediately close to the surface in the space and airborne configurations, respectively.

b. Single vertical profile analyses

To understand better the MS effects at 35.5 GHz in the EGPM configuration, five vertical profiles are analyzed in more detail (Figs. 10–14). For each profile, the vertical distribution of the hydrometeor (top panels), the SS properties (center panels), and the SS and MS reflectivities (bottom panels) are drawn. Figures 10–11

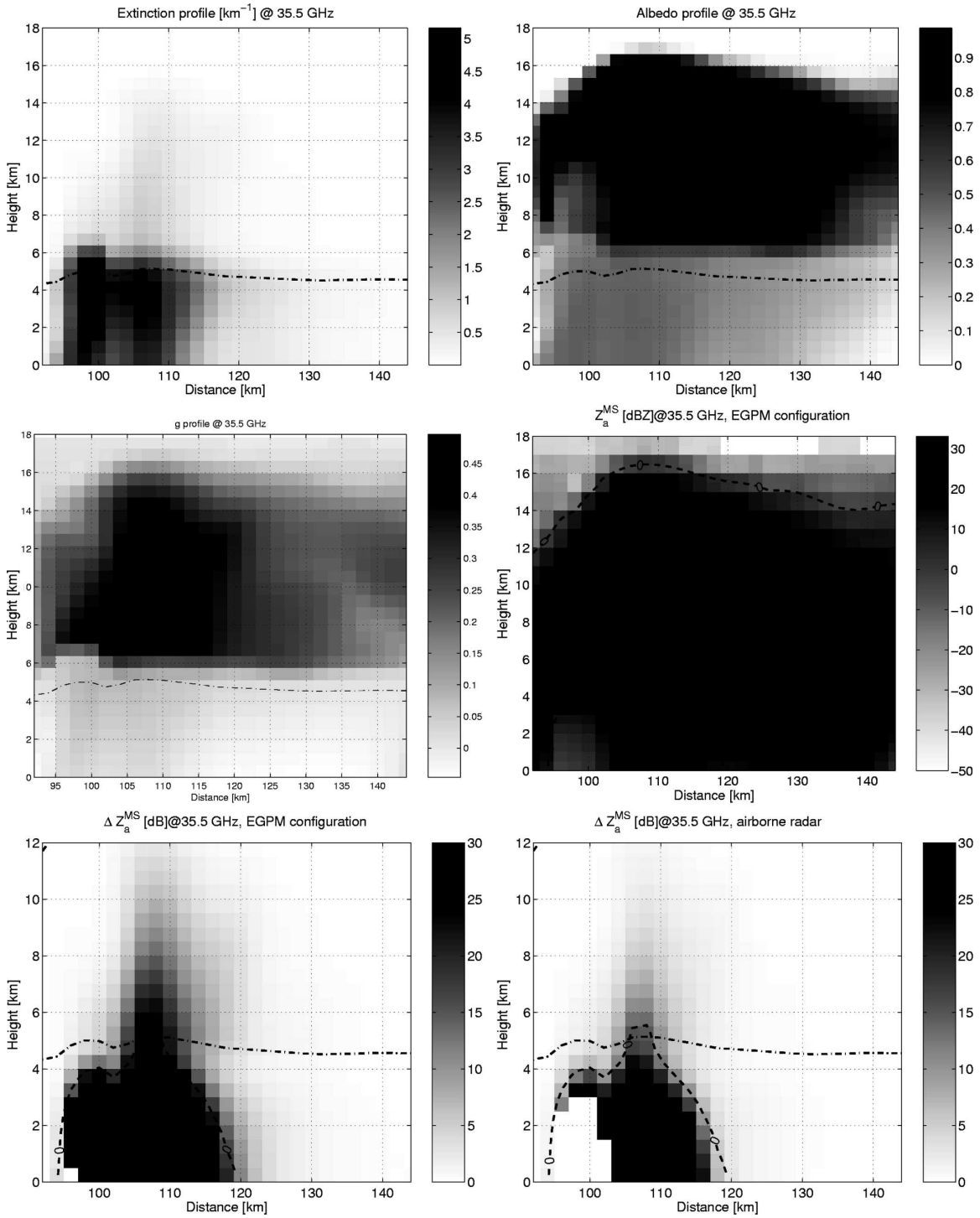

FIG. 7. Same as Fig. 5, but for the LBA cross section in the south–north direction at $x = 134$ km. The corresponding hydrometeor density profile is shown in the top-right panel of Fig. 3.

show two vertical profiles corresponding to heavy rain, which were extracted from the profile shown in the top-left panel of Fig. 4 at $x = 134$ and $x = 198$ km. The profile in Fig. 10 contains a considerable amount of graupel particles ("cold rain" case); in Fig. 11, the only hydrometeors present in the profile are in the liquid phase ("warm rain" case). In terms of MS, this makes a huge difference: in fact, the graupel layer in the cold-

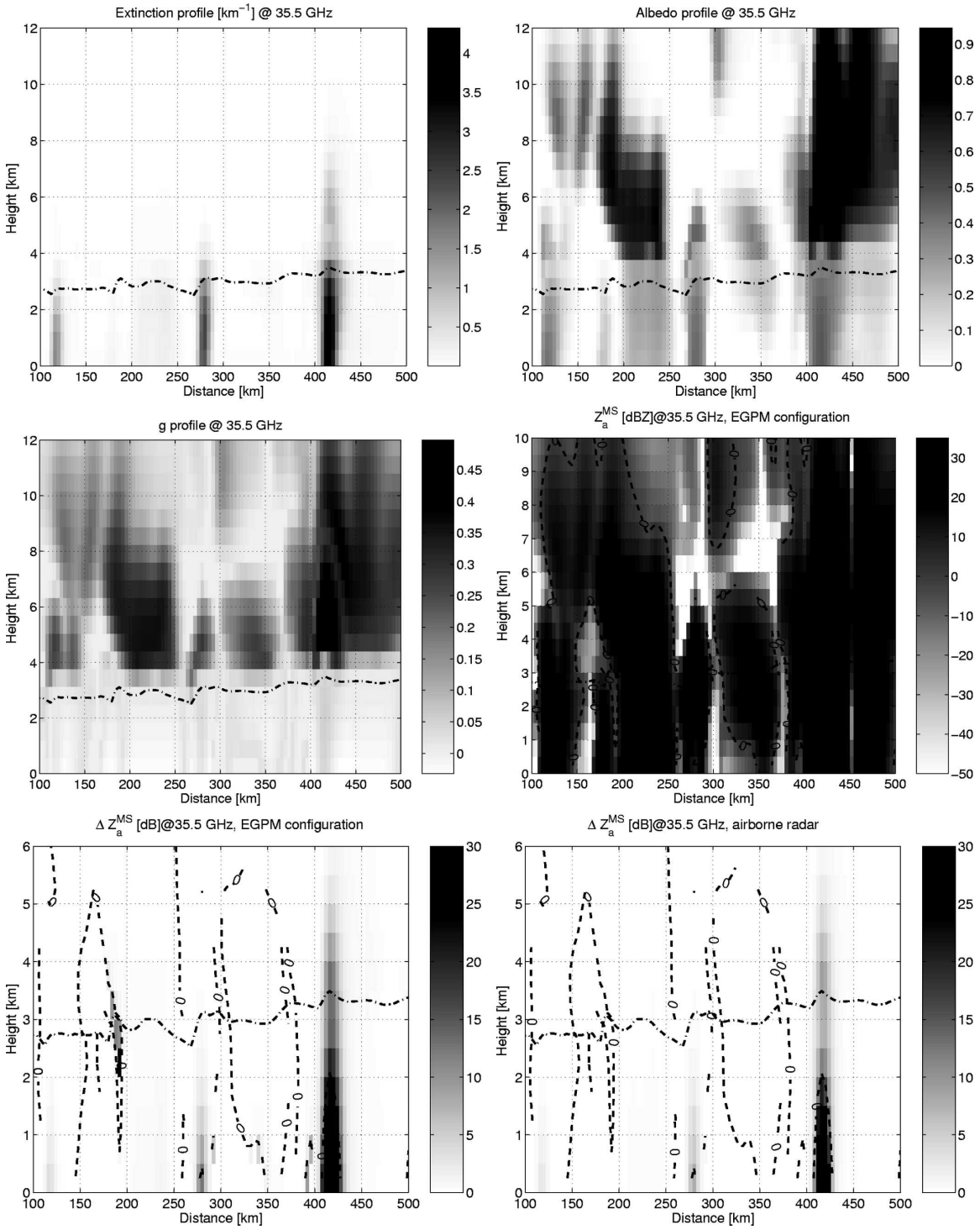

FIG. 8. Same as Fig. 5, but for the CF cross section. The corresponding hydrometeor density profile is shown in the bottom-left panel of Fig. 3.

rain profile (Fig. 10) represents an effective scattering layer, that is, a source of MS. This is totally absent in the warm-rain profile of Fig. 11. As a consequence, in the cold-rain case, the signal seemingly coming from deep inside the rain layer is actually created by photons that have traveled considerably and have been scattered many times inside the scattering medium represented by the graupel core. In the bottom panel of Fig.

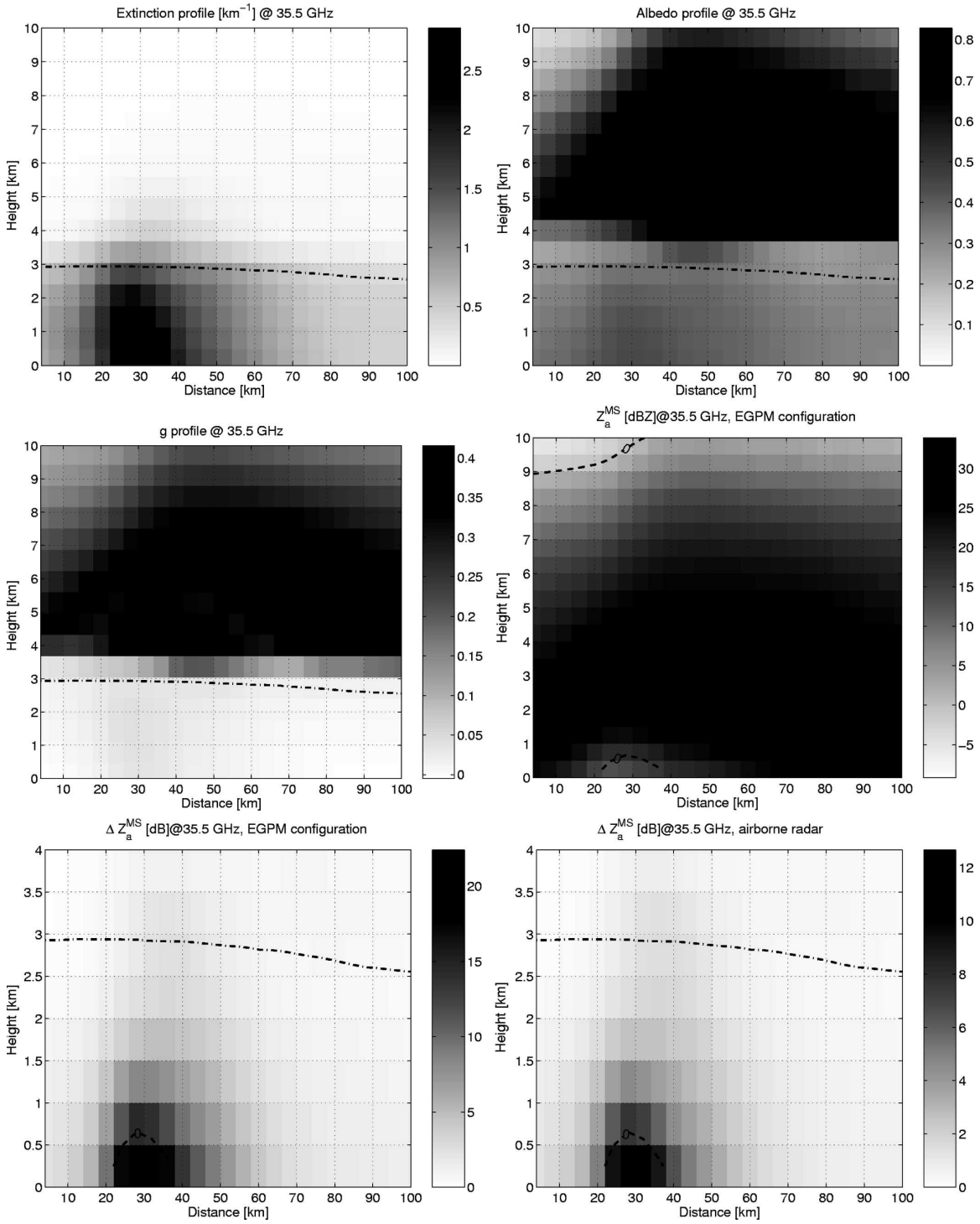

FIG. 9. Same as Fig. 5, but for the WF cross section. The corresponding hydrometeor density profile is shown in the bottom-right panel of Fig. 3.

10, the departure from the SS reflectivities [defined by Eq. (1) and obtained by subtracting the two curves in the bottom panel of Fig. 10] increases with increasing range and it gives an increment of over 30 dB close to the surface. On the other hand, the warm-rain scenario (Fig. 11) has a maximum MS enhancement close to the ground of less than 4 dB. A similar dichotomy between cold rain and warm rain is shown for the CF simulation

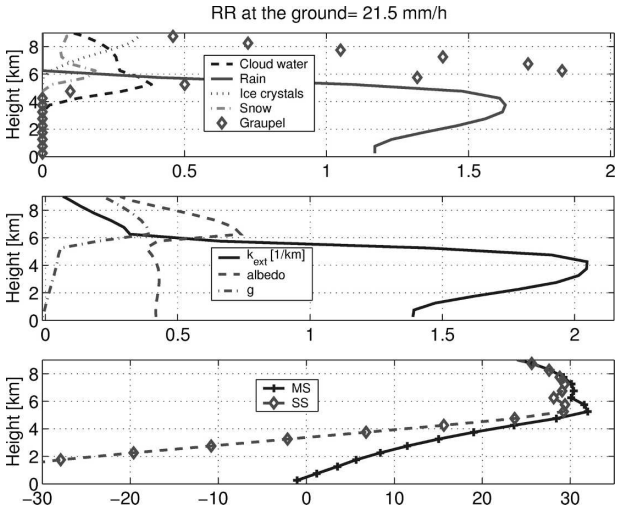

FIG. 10. Deep convection in the SL simulation: (top) hydrometeor content (g m^{-3}), (middle) SS properties at 35.5 GHz, and (bottom) 35.5-GHz Z_a^{MS} and Z_a^{SS} profiles (dBZ) for the EGPM spaceborne configuration (0.5° beamwidth and altitude of 600 km).

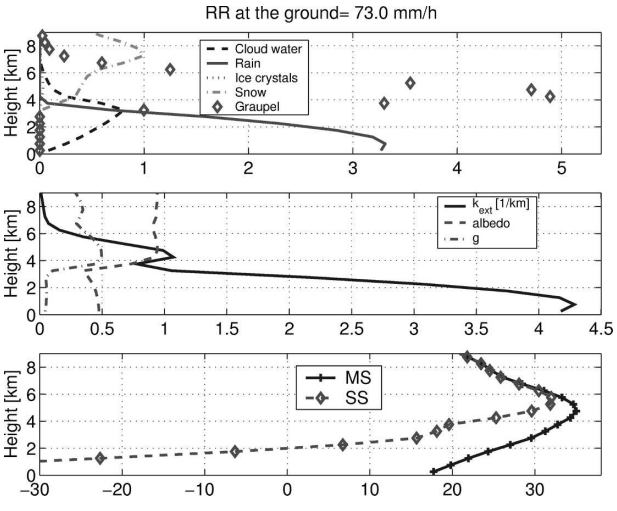

FIG. 12. Same as Fig. 10, but for deep convection in the CF simulation.

in Figs. 12–13, which present the profiles at $x = 116$ and $x = 416$ km, respectively, extracted from the cross section depicted in the top-left panel of Fig. 8. Note that cold-rain profiles in stratiform conditions are likely to be characterized by a bright band as well. Though the melting layer never exceeds 1 km, it is generally responsible for an increase in the scattering properties (e.g., the brightband phenomenon). As such, it is an additional factor that will enhance MS effects.

Last, in Fig. 14, a profile containing a snow layer above a layer of low rain (but clear sky between) is shown (it corresponds to $x = 192$ km in the top-left panel of Fig. 8). This demonstrates an example of the difficulties introduced by MS effects when evaluating the bottom of cloud layers. In fact, because of the MS signal, the snow layer looks thicker than it really is, which is an effect already observed in lidar simulations and predicted in section 6 of Part I.

c. Discussion

The results shown here are consistent with the expectations from the analyses performed in Part I on the basis of a much simpler setup. Multiple scattering essentially increases with the increase of the scattering optical depth traveled by the electromagnetic waves inside the scattering medium. To highlight this feature,

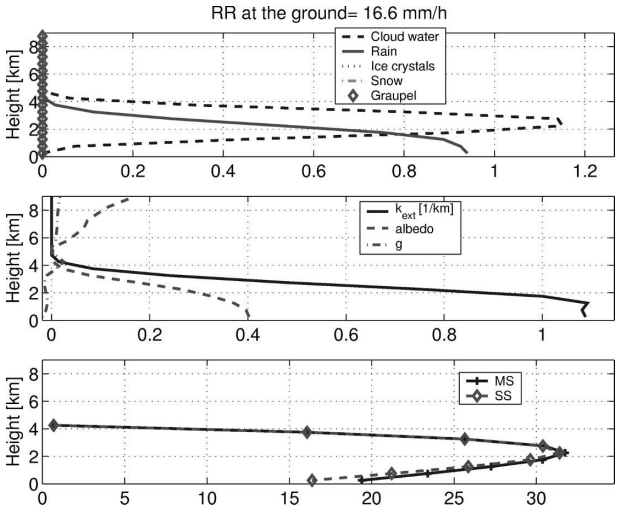

FIG. 11. Same as Fig. 10, but for warm rain in the SL simulation.

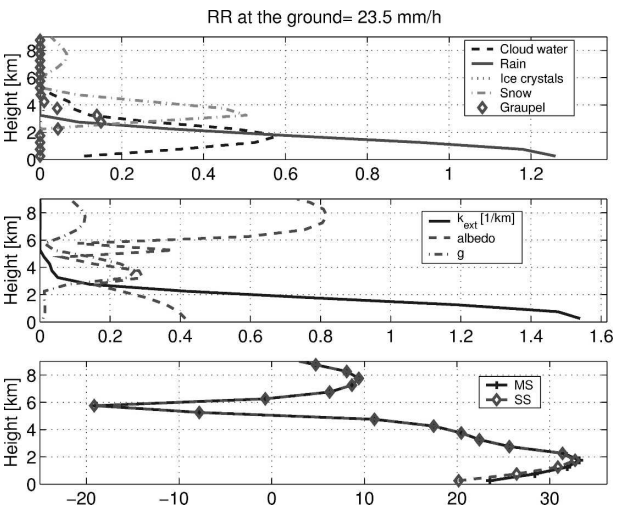

FIG. 13. Same as Fig. 10, but for warm rain in the CF simulation.

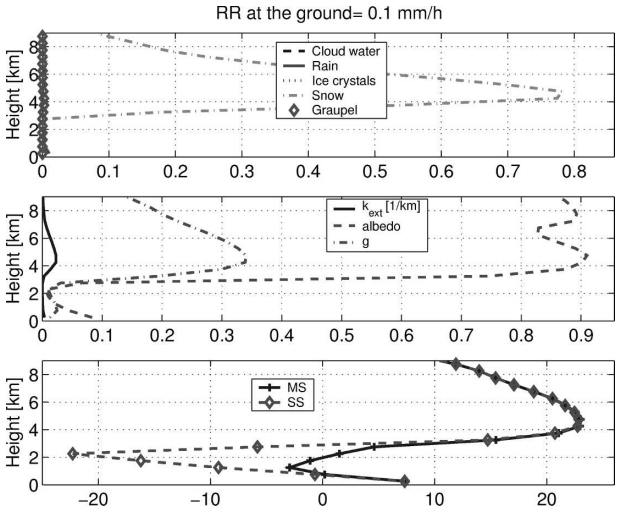

FIG. 14. Same as Fig. 10, but for a vertical profile containing a snow layer in the CF simulation.

Fig. 15 shows ΔZ_a^{MS} as defined by Eq. (1) in spaceborne configuration. Each point of the scatterplot corresponds to one pixel of the profiles of the analyzed CRMs. The results fit very well with those depicted in Fig. 10 in Part I. The scatter for each given scattering optical depth has to be ascribed to the inhomogeneity of the different profiles (which can generally have different k_{ext} profiles and different phase functions). These plots are valuable for providing a rough estimate of the MS that one can expect once a certain scattering profile is given.

In particular, when looking at the top panel of Fig. 15 we can conclude that when realistic antenna footprints and minimum detection thresholds envisaged for the GPM precipitation radars are considered, MS effects are generally negligible at 13 GHz in comparison with other uncertainties involved in retrieval problems. The only points at which the MS signal is higher than 2.5 dB are those associated with the LBA simulation. As previously discussed in section 3, that cross section relates to a very strong convective case over tropical land and has to be considered as an extreme scenario.

At 35.5 GHz the MS signal really becomes an issue ($\geq$5 dB) when scattering optical depths higher than 1 are traveled by the signal inside the medium. The MS can result in increments of 20 dB at scattering penetration depths of 2.5. The scattering optical depth traveled inside the medium by the electromagnetic waves obviously plays a major role in MS effects. This highlights the importance of ice hydrometeors with high density (like graupel or, even better, hail) that—by providing both a highly scattering environment and an optically thick layer—can result in a high scattering optical thickness $\varpi\tau$.

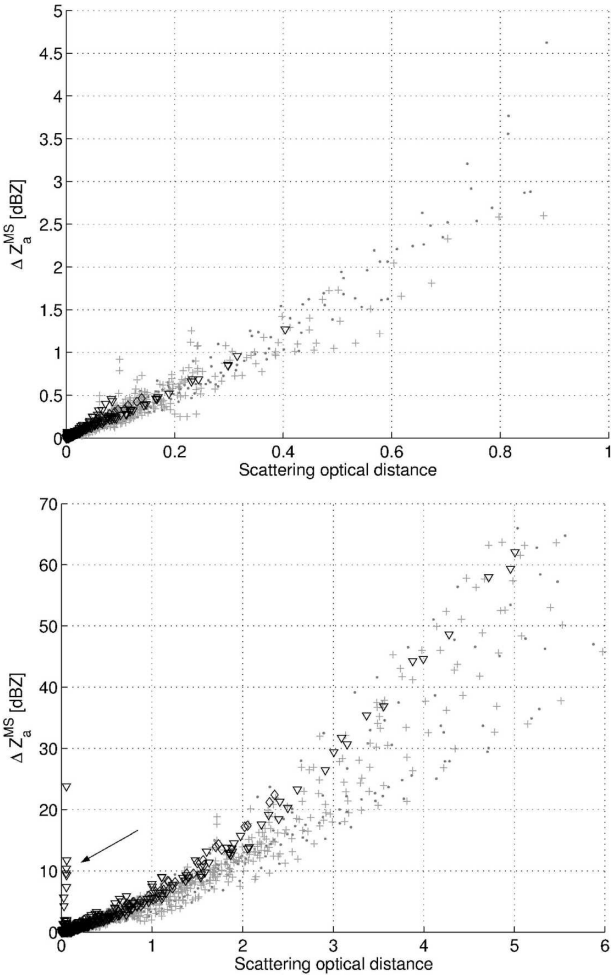

FIG. 15. MS effect vs scattering optical depth inside the medium for (top) 13.8 and (bottom) 35.5 GHz. The PR and EGPM configuration have been selected. Different symbols correspond to different CRM simulations: LBA (dots), SL (crosses), WF (diamonds), and CF (triangles).

Last, note that the isolated points with very small scattering optical distance and high MS enhancement in the bottom panel of Fig. 15 (see arrow) correspond to profiles similar to that shown in Fig. 14; that is, they represent MS signals from the sharp edge of the bottom of thin ice layers.

4. Airborne campaigns and validation of MS effects

The results presented here can be extended to larger and more representative databases to develop retrieval algorithms. However, we deem it mandatory to first demonstrate the validity of the simulated MS effects. In analogy to what has already been done with lidars (e.g., Sassen and Petrilla 1986; Sassen 2000; Cahalan et al. 2005), two ideas can be explored: 1) performance of simultaneous reflectivity measurements with different

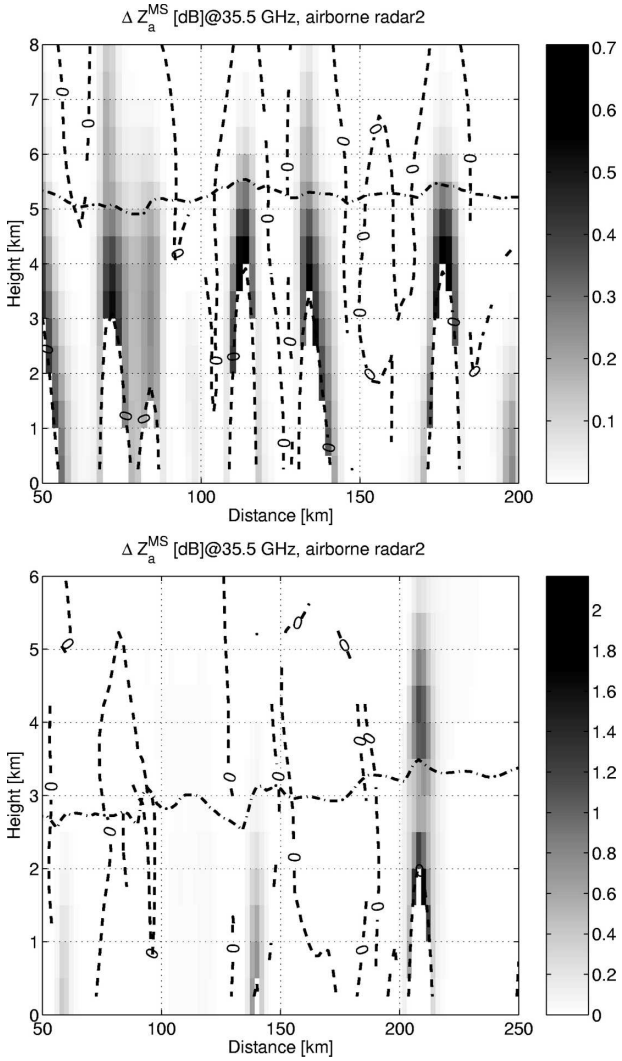

FIG. 16. The ΔZ_a^{MS} corresponding to the SL and CF hydrometeor profiles (top-left and bottom-left panels of Fig. 3, respectively) for an airborne configuration different from that previously adopted in the bottom-right panels of Fig. 5 and Fig. 8. Here the 35.5-GHz radar flies at 20-km altitude as well, but with a 0.5°-beamwidth dish. The dashed lines represent the 0-dBZ MS reflectivity contour level.

fields of view and 2) performance of measurements of the cross-polarized component of the received signal. From the point of view of an airborne campaign, the first option can be realized using a radar with two antennas. In both signals, the MS should be much higher for the smaller dish. Figure 16 shows as an example ΔZ_a^{MS} for the SL overpass (see top-left panel of Fig. 3) and for the CF overpass (see bottom-left panel of Fig. 3) simulations for a 35.5-GHz airborne radar with a 0.5° beamwidth dish flying at 20-km altitude. These two panels have to be compared with the two bottom-right panels of Fig. 5 and Fig. 8, which are obtained with the same configuration but with a 4.8° antenna beamwidth. The MS effects are very different for the two configurations. For instance, when looking at the lower part of the strong convective cell around $x = 410$ km in the CF ($x = 70$ km in the SL), the readings from the two airborne radars should differ by more than 30 (12) dB. Obviously, an intercomparison between the readings of the two radar systems will not be so straightforward because of the presence of beam-filling effects. For instance, at 5 km above the ground (15 km below the flight height), the bigger footprint (associated with the smaller antenna) will have a radius on the order of 1.25 km while the 0.5° beamwidth dish will have a radius that is smaller by a factor of almost 10.

For the second option, the configuration seems more practical because it involves polarization capabilities, which are easier to accommodate. In contrast to Z_a^{SS}, strong cross-polarized components are expected in Z_a^{MS}. In fact, the signal from photons experiencing scattering orders higher than 1 tends to be unpolarized or at least to forget the impinging polarization state. Therefore, the MS components have strong contributions also from the cross-polar channel (and not only from the copolar one). This should produce "unexpected" high values for LDR both at the rear edge of clouds (resulting from the thicker appearance of clouds by MS; see the discussion in section 5c of Part I) and from ranges corresponding to high scattering optical depth where the signal has strong MS components. These LDR features can hardly be explained from the SS point of view. Even at higher frequencies, reported LDR observations (e.g., Wolde and Vali 2001) of graupel at close distance (which are not affected by propagation and MS effects) do not exceed −6 dB at side view and −9 dB when nadir looking. This contrasts with lidar MS polarization effects, which can often be jeopardized by SS nonspherical-hydrometeor cross-polar return (Sassen 2000).

As an example, Fig. 17 shows the $\mathrm{LDR}_{hv}^{\mathrm{MS}} \equiv z_{hv}^{\mathrm{MS}}/z_{vv}^{\mathrm{MS}}$ as computed from our code for a 35-GHz radar with a half-power beamwidth equal to 4.8° flying at 20 km over the LBA and the CF cross sections depicted in the top-right and bottom-left panels of Fig. 3, respectively. For a K_u-band radar, the results for LDR (not shown) look qualitatively like those in Fig. 17 but are typically 10 dB lower. Because the medium is supposed to be composed of spherical hydrometeors, no $\mathrm{LDR}_{hv}^{\mathrm{SS}}$ is expected (the same is true even when nonspherical particles that are horizontally aligned are considered when radars are operated in nadir-looking conditions). On the other hand, the region where significant MS is present is characterized by significantly high values of the cross-polarized signal (up to 0 dB).

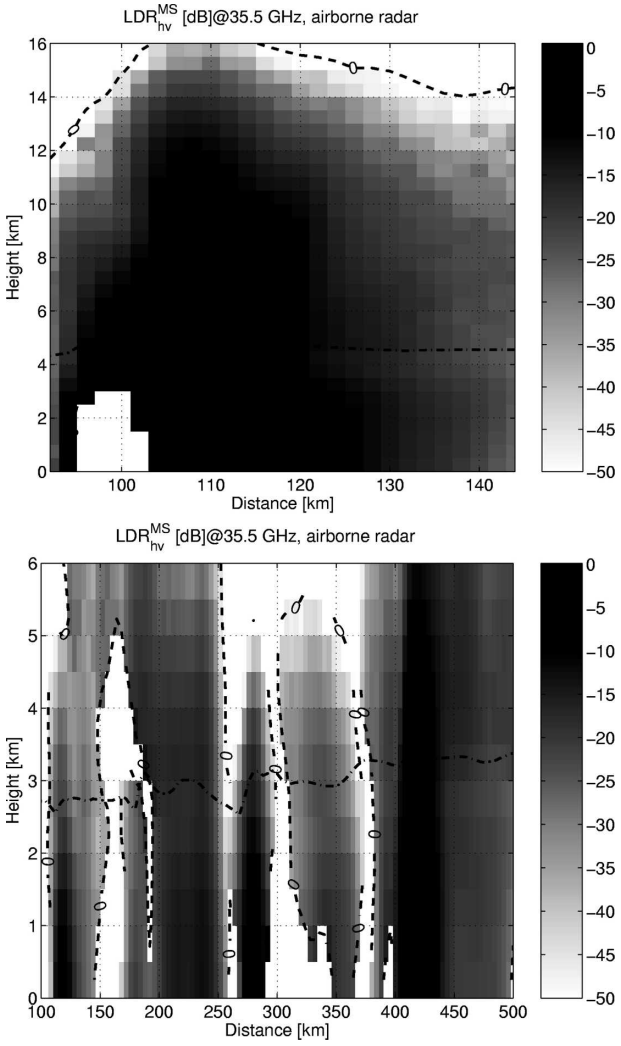

FIG. 17. LDR$_{hv}^{MS}$ corresponding to the (top) LBA and (bottom) CF hydrometeor profiles (top-right and bottom-left panels of Fig. 3, respectively) for the same airborne configuration previously adopted in the bottom-right panels of Fig. 7 and Fig. 8. The dashed lines represent the 0-dBZ MS reflectivity contour level.

The same general LDR behavior can be found for the other simulations as well, but the LDR signal is generally not as high: values in the range of $(-10, -5)$ dB are commonly found in the vicinity of rain cores underneath thick ice layers at 35.5 GHz. It is obvious that when the airplane is flying closer to the ground and/or with a bigger antenna dish the LDR values are lower than those expected with a footprint at the ground equal to 1.7 km. LDR signatures are very distinctive MS effects, whereas a reflectivity enhancement can be masked by many other effects. Thus, the detection of the cross-polarized radiation can provide a very good estimate of the MS effect and therefore can be a key quantity to be incorporated into retrieval algorithms. For instance, one can imagine selecting a

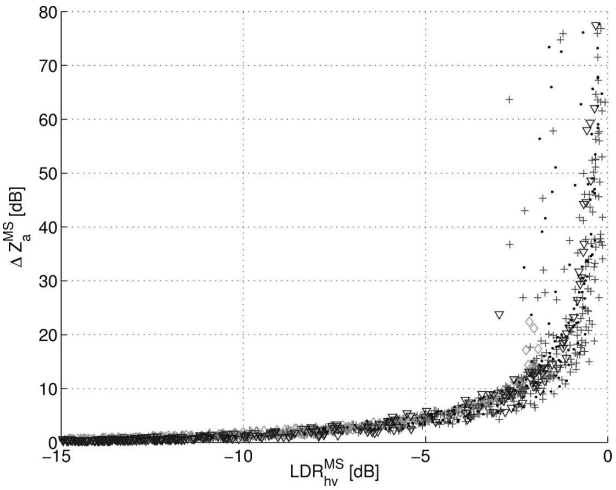

FIG. 18. Linear depolarization ratio vs MS enhancement at 35.5 GHz in the EGPM configuration. Different symbols correspond to different CRM simulations: LBA (dots), SL (crosses), WF (diamonds), and CF (triangles).

threshold for the LDR$_{hv}$ above which MS effects provide substantial change in the reflectivity. This is easily demonstrated in Fig. 18 where a scatterplot of LDR$_{hv}$ versus ΔZ_a^{MS} evaluated at 35.5 GHz in the EGPM configuration is shown. Values of LDR$_{hv} < -13$ dB (-10 dB) guarantee $\Delta Z_a^{MS} < 1$ dB ($\Delta Z_a^{MS} < 2$ dB).

In this context, it is noteworthy to recall that some airborne measurements conducted in the early 1990s (e.g., Iguchi et al. 1992; or see Fig. 4 in Ito et al. 1995) did reveal the presence of high LDR values in areas of convective rain, which cannot be due to SS even if large, deformed raindrops are assumed. The *hh* and *hv* (horizontal emitting–horizontal receiving and horizontal emitting–vertical receiving, respectively) configurations have been adopted more recently in the second-generation Airborne Precipitation Radar (APR-2; see http://trmm.jpl.nasa.gov/apr.html), which is a prototype for the GPM rain profiling radar (Sadowy et al. 2003). APR-2 is capable of making simultaneous measurements of rainfall parameters, including copolarized and cross-polarized rain reflectivities and vertical Doppler velocities. Since August 2001, APR-2 has been deployed on the National Aeronautics and Space Administration (NASA) P3 and DC8 aircrafts in four experiments, including the Convection and Moisture Experiment (CAMEX)-4 and the Wakasa Bay Experiment. LDR data from these campaigns are actually available only for the K_u band (Im 2003). This is because LDR requires interchannel calibration and the K_a band still has moderate uncertainty. Moreover, artificially high LDR values are often present in the vicinity of cloud boundaries because of the low signal-to-noise ratio in these areas. Because of these problems, these data have

not been fully analyzed for evidence of MS signatures in LDR signals. However, when 94-GHz data from the Airborne Cloud Radar are considered, these signatures show up (Battaglia et al. 2005b). As demonstrated above, these signatures are stronger when larger-footprint and higher-scattering optical systems are considered so that they are more likely to be present when observations are made from upper-tropospheric airborne systems flying over tall systems.

5. Discussion and conclusions

The numerical Monte Carlo model developed in Part I has been exploited to evaluate the MS effects in realistic scenarios (including both tropical and midlatitude rainy systems) for 13- and 35-GHz radars both in space and in airborne configuration. The MS effects have been characterized in terms of the MS reflectivity enhancement ΔZ_a^{MS} and of the linear depolarization ratio $\mathrm{LDR}_{hv}^{\mathrm{MS}}$. When the copolarized reflectivity is considered, the MS enhancement becomes a real issue for K_a band radars. At 13 GHz, even in spaceborne configuration, the effect never exceeds a few decibels, even in the more extreme scenarios. It is crucial to observe that 30 kg m^{-2} (like found in the LBA simulation) are pretty extreme values. Recent studies (Lang et al. 2006) suggest that there is commonly a considerable high bias of water contents (and graupel, in particular) that are simulated by cloud-resolving-model simulations (in particular by GCE) that rely on standard bulk microphysics schemes. Because MS effects depend upon the scattering optical depth and are most pronounced when deep columns of graupel are present, these scenarios are believed to be very rarely met in operational measurements.

On the other hand, for 35.5-GHz radars in typical spaceborne configurations, the ΔZ_a^{MS} can reach tens of decibels. This is particularly true when cold rain systems are considered, that is, rain layers with high-density ice particles aloft. A key parameter to forecast the total magnitude of the effect is provided by the scattering optical thickness [see Eq. (19) in Part I]. In cold-rain conditions the MS effects may have been overestimated because of the high ice contents of the analyzed hydrometeor profiles; however, MS is believed to remain consistent and not negligible at the K_a band. This will obviously affect dual-wavelength spaceborne radar retrievals (e.g., Kuo et al. 2004; Haddad et al. 2006). The identification of the presence of MS is a troublesome problem, especially when no cross-polarized signal is detected, like in GPM configuration (Iguchi et al. 2002). In fact, our computations show that MS effects are unambiguously detected when cross-polar signals are considered. The $\mathrm{LDR}_{hv}^{\mathrm{MS}}$ is much stronger than the $\mathrm{LDR}_{hv}^{\mathrm{SS}}$ and should provide clear signatures with high LDR in regions where high ΔZ_a^{MS} are located (see Fig. 18). We predict LDR values even higher than -5 dB when considering typical spaceborne systems. When passing to airborne systems, the effect is obviously much reduced. An intercomparison with real airborne data is mandatory for future work and ad hoc field campaigns are recommended for this purpose.

From a GPM perspective, any MS effect that increases the apparent reflectivity by several decibels would render most retrieval algorithms using the K_a-band data less accurate than the K_u-band-only retrieval, unless a correction is made. For this reason, two main scenarios are possible: the first one in which both radars detect a single from the surface and the second one in which only the K_u-band radar detects a signal from the surface. In the first case, a sophisticated inversion framework should be possible, by essentially mimicking the surface reference technique (Iguchi et al. 2000; Meneghini et al. 2000, 2004) with the constraint that the surface return provide information about the MS enhancement from the surface bin, that is, the MS produced by the total atmospheric column. At 35.5 GHz (and to a smaller extent also at 13 GHz) the surface return will be enhanced by the MS contribution from the upper layers so that the apparent path attenuation will be actually reduced with respect to the path attenuation as computed with the usual SS approximation. The idea is well described in section 3c of Marzano et al. (2003) for the K_u band, but it should be straightforward to extend it to dual-wavelength retrieval schemes. However, especially when considering the typical MDT (see column six in Table 1), the 35-GHz radar will never see the surface for intense or heavy precipitation. In these cases, the quantification of MS is believed to be very difficult (and it will generally cause high instabilities like the classical Hitschfeld–Bordan solution) and the use of the K_u radar should be the only feasible option.

As a follow-on to this study, we plan to investigate MS effects in spaceborne radars planned to operate at 94 GHz, with particular attention to be paid to the CloudSat configuration. It will also be interesting to consider the relevance of this MS effect for ground-based radar meteorology. In this case, MS effects will be damped by the presence of much smaller backscattering volumes and the fact that the radar beam meets first the more absorbing rain portion and then the more scattering ice part. Our code also allows polarimetric quantities to be investigated so that it can be used to evaluate MS effects in polarimetric signatures like those explained in Hubbert and Bringi (2000). Last, the model is flexible enough to incorporate the whole 3D

structure of the storm and to include layers with melting particles.

Acknowledgments. Doctor Ajewole is grateful to the Alexander von Humboldt Foundation, the University of Bonn, and the Federal University of Technology of Akure for the research visit to Germany. The authors thank Dr. Kummerow at CSU, Dr. W. K. Tao, and all of his colleagues at NASA GSFC for making the cloud-resolving-model simulations available. The suggestions and comments by the anonymous reviewers are gratefully acknowledged.

REFERENCES

Battaglia, A., M. O. Ajewole, and C. Simmer, 2005a: Multiple scattering effects due to hydrometeors on precipitation radar systems. *Geophys. Res. Lett.,* **32,** L19801, doi:10.1029/2005GL023810.

——, ——, and ——, 2005b: When does multiple scattering due to hydrometeors become relevant to space-borne radar measurements? Preprints, *32d Conf. on Radar Meteorology,* Albuquerque, NM, Amer. Meteor. Soc., CD-ROM, P1R.13.

——, ——, and ——, 2006: Evaluation of radar multiple scattering effects from a GPM perspective. Part I: Model description and validation. *J. Appl. Meteor. Climatol.,* **45,** 1634–1647.

Cahalan, R. F., M. McGill, J. Kolasinski, T. Varnai, and K. Yetzer, 2005: THOR—Cloud thickness from offbeam lidar returns. *J. Atmos. Oceanic Technol.,* **22,** 605–627.

Durden, S. L., E. Im, Z. S. Haddad, and L. Li, 2003: Comparison of TRMM precipitation radar and airborne radar data. *J. Appl. Meteor.,* **42,** 769–774.

Geerts, B., and Y. Dawei, 2000: Classification and characterization of tropical precipitation based on high-resolution airborne vertical incidence radar. Part I: Classification. *J. Appl. Meteor.,* **43,** 1554–1566.

Haddad, Z. S., J. P. Meagher, S. L. Durden, E. A. Smith, and E. Im, 2006: Drop size ambiguities in the retrieval of precipitation profiles from dual-frequency radar measurements. *J. Atmos. Sci.,* **63,** 204–217.

Heymsfield, G. M., B. Geerts, and L. Tian, 2000: TRMM precipitation radar reflectivity profiles as compared with high-resolution airborne and ground-based radar measurements. *J. Appl. Meteor.,* **39,** 2080–2102.

Hong, Y., J. L. Haferman, W. S. Olson, and C. D. Kummerow, 2000: Microwave brightness temperatures from tilted convective systems. *J. Appl. Meteor.,* **39,** 983–998.

Hubbert, J., and V. N. Bringi, 2000: The effects of three-body scattering on differential reflectivity signatures. *J. Atmos. Oceanic Technol.,* **17,** 51–61.

Iguchi, T., R. Meneghini, and H. Kumagai, 1992: Radar depolarization signatures of rain in cumulus clouds measured with a dual-frequency air-borne radar. *Geoscience and Remote Sensing Symp.,* Vol. 2, Houston, TX, IGARSS, 1728–1730.

——, T. Kozu, R. Meneghini, J. Awaka, and K. Okamoto, 2000: Rain-profiling algorithm for the TRMM precipitation radar. *J. Appl. Meteor.,* **39,** 2038–2052.

——, R. Oki, E. A. Smith, and Y. Furuhama, 2002: Global precipitation measurement program and the development of dual-frequency precipitation radar. *J. Comm. Res. Lab.,* **49,** 37–45.

Im, E., cited 2003: APR-2 dual-frequency airborne radar observations, Wakasa Bay, Japan. National Snow and Ice Data Center. [Available online at http://nsidc.org/data/nsidc-0195.html.]

Ingmann, P., 2004: EGPM–European Global Precipitation Measurement technical and programmatic annex. Reports for Mission Selections, ESA, ESTEC, Tech. Rep. SP-1279 (5), 66 pp.

Ito, S., T. Oguchi, T. Iguchi, H. Kumagai, and R. Meneghini, 1995: Depolarization of radar signals due to multiple scattering in rain. *IEEE Trans. Geosci. Remote Sens.,* **33,** 1057–1062.

Kobayashi, S., S. Tanelli, T. Iguchi, and E. Im, 2004: Backscattering enhancement with a finite beam width for millimeter-wavelength weather radars. *Microwave Remote Sensing of the Atmosphere and Environment IV,* G. S. Jackson and S Uratsuka, Eds., International Society for Optical Engineering (SPIE Proceedings Vol. 5654), 106–113.

Kummerow, C. D., W. Barnes, T. Kozu, J. Shiue, and J. Simpson, 1998: The Tropical Rainfall Measuring Mission (TRMM) sensor package. *J. Atmos. Oceanic Technol.,* **15,** 809–817.

Kuo, K.-S., E. A. Smith, Z. Haddad, E. Im, T. Iguchi, and A. Mugnai, 2004: Mathematical–physical framework for retrieval of rain DSD properties from dual-frequency Ku–Ka-band satellite radar. *J. Atmos. Sci.,* **61,** 2349–2369.

Lang, S., W.-K. Tao, R. Cifelli, W. Olson, J. Halverson, S. Rutledge, and J. Simpson, 2006: Improving simulations of convective systems from TRMM LBA: Easterly and westerly regimes. *J. Atmos. Sci.,* in press.

Lhermitte, R., 1990: Attenuation and scattering of millimeter wavelength radiation by clouds and precipitation. *J. Atmos. Oceanic Technol.,* **7,** 464–479.

Marshall, J. S., and W. M. Palmer, 1948: The distribution of raindrop with size. *J. Meteor.,* **5,** 165–166.

Marzano, F. S., L. Roberti, S. Di Michele, A. Mugnai, and A. Tassa, 2003: Modeling of apparent radar reflectivity due to convective clouds at attenuating wavelenghts. *Radio Sci.,* **38,** 1002, doi:10.1029/2002RS002613.

Meneghini, R., T. Iguchi, T. Kozu, L. Liao, K. Okamoto, J. A. Jones, and J. Kwiatkowski, 2000: Use of the surface reference technique for path attenuation estimates from the TRMM precipitation radar. *J. Appl. Meteor.,* **39,** 2053–2070.

——, J. A. Jones, T. Iguchi, K. Okamoto, and J. Kwiatkowski, 2004: A hybrid surface reference technique and its application to the TRMM precipitation radar. *J. Atmos. Oceanic Technol.,* **21,** 1645–1658.

Sadowy, G. A., A. C. Berkun, W. Chun, E. Im, and S. L. Durden, 2003: Development of an advanced airborne precipitation radar. *Microwave J.,* **46,** 84–98.

Sassen, K., 2000: Lidar backscatter depolarization technique. *Light Scattering by Nonspherical Particles: Theory, Measurements, and Applications,* M. I. Mishchenko, J. W. Hovenier, and L. D. Travis, Eds., Academic Press, 393–416.

——, and R. L. Petrilla, 1986: Lidar depolarization from multiple scattering in marine stratus clouds. *Appl. Opt.,* **25,** 1450–1459.

Tao, W. K., and J. Simpson, 1993: Goddard Cumulus Ensemble model. Part I: Model description. *Terr. Atmos. Oceanic Sci.,* **4,** 35–72.

Tao, W.-K., and Coauthors, 2003: Microphysics, radiation and surface processes in the Goddard Cumulus Ensemble (GCE) model. *Meteor. Atmos. Phys.,* **82,** 97–137.

Wolde, M., and G. Vali, 2001: Polarimetric signatures from ice crystals observed at 95 GHz in winter clouds. Part I: Dependence on crystal form. *J. Atmos. Sci.,* **58,** 828–841.